communications materials

Article

https://doi.org/10.1038/s43246-024-00513-4

Tunable magnetism in titanium-based kagome metals by rare-earth engineering and high pressure

Long Chen[1,2,5], Ying Zhou[1,2,5], He Zhang[1,2,5], Xuecong Ji[1,2,5], Ke Liao[1,2], Yu Ji[1,2], Ying Li[1], Zhongnan Guo[3], Xi Shen[1], Richeng Yu[1,2,4], Xiaohui Yu[1,2,4] ✉, Hongming Weng[1,2,4] ✉ & Gang Wang[1,2,4] ✉

Rare-earth engineering is an effective way to introduce and tune magnetism in topological kagome materials, which have been acting as a fertile platform to investigate the quantum interactions between geometry, topology, spin, and correlation. Here, we report the synthesis, structure, and physical properties of titanium-based kagome metals $RETi_3Bi_4$ (RE = Yb, Pr, and Nd) with various magnetic states. They all crystallize in the orthogonal space group *Fmmm* (No. 69), featuring distorted titanium kagome lattices and rare-earth zig-zag chains. By changing the rare earth atoms in the zig-zag chains, the magnetism can be tuned from nonmagnetic $YbTi_3Bi_4$ to short-range ordered $PrTi_3Bi_4$ ($T_{anomaly}$ ~ 8.2 K), and finally to ferromagnetic $NdTi_3Bi_4$ (T_c ~ 8.5 K). In-situ resistance measurements of $NdTi_3Bi_4$ under high pressure further reveal a tunable ferromagnetic ordering temperature. These results highlight $RETi_3Bi_4$ as a promising family of kagome metals to explore nontrivial band topology and exotic phases.

Topological kagome materials have attracted tremendous attention in the past decades, serving as a fundamental platform to investigate the quantum interactions between geometry, topology, spin, and correlation[1]. From Heisenberg's view[2], magnetic ions on the kagome lattice with antiferromagnetic interaction would exhibit geometrical frustration[3], resulting in possible quantum-spin-liquid states[4], fractionalized excitations[5], and the absence of ordinary magnetic order[6,7]. When focusing on the electronic structure of kagome lattices with magnetic ions, the strong electron correlation originating from the flat band would stabilize a ferromagnetic (FM) ground state[8]. Moreover, with Dirac fermions and van Hove singularities in the electronic structure, kagome lattices would show nontrivial topological properties[9,10] and multiple long-range orders with instabilities of Fermi surface[11]. By introducing the magnetic degree of freedom, correlated topological band structures can be realized in kagome lattices with magnetic ions, known as topological kagome magnets. Theoretically, the inclusion of spin-orbit coupling in the kagome lattice would open gaps at the Dirac point and the touching point connecting the flat band and the quadratic band, making the nonmagnetic kagome lattice a quantum spin Hall insulator with nontrivial Z_2 topological invariants[12,13]. Thus, a kagome lattice with magnetic ions showing out-of-plane FM ordering would become a Chern insulator with chiral edge states, which usually exhibits exotic quantum properties such as quantized anomalous Hall effect[14] and giant anomalous Hall conductance[15,16]. Moreover, a large in-plane magnetization would close the gaps in topological kagome magnets, acting as a tuning parameter for topological phases[1]. Considering the strong or weak interlayer interaction, Weyl point[17–19] or three-dimensional quantum anomalous Hall effect[20] is anticipated to appear in topological kagome magnets. Due to these exotic quantum properties, topological kagome magnets have great potential applications for next-generation electronics, and it is essential to explore more topological kagome magnets and investigate their properties.

Experimentally, there are two strategies to introduce magnetism into kagome materials, placing magnetic ions on the kagome lattice or intercalating magnetic ions between stacked kagome lattices. Plenty of topological kagome magnets have been reported with magnetic transition metal ions on the kagome lattice, such as Mn_3X (X = Sn, Ge) with a manganese-kagome lattice[21–23], $Co_3Sn_2S_2$[24–26] and CoSn[27,28] with a cobalt-kagome lattice, Fe_3Sn_2[16,29,30] and FeSn[31–33] with an iron-kagome lattice, most of which have strong in-plane magnetization. In $REMn_6Sn_6$ (RE = Gd-Tm, Lu) with

[1]Beijing National Laboratory for Condensed Matter Physics, Institute of Physics, Chinese Academy of Sciences, Beijing 100190, China. [2]University of Chinese Academy of Sciences, Beijing 100049, China. [3]Department of Chemistry, School of Chemistry and Biological Engineering, University of Science and Technology Beijing, Beijing 100083, China. [4]Songshan Lake Materials Laboratory, Dongguan, Guangdong 523808, China. [5]These authors contributed equally: Long Chen, Ying Zhou, He Zhang, Xuecong Ji. ✉e-mail: yuxh@iphy.ac.cn; hmweng@iphy.ac.cn; gangwang@iphy.ac.cn

manganese-kagome lattice, various magnetic states can be realized by substitution of rare-earth atoms, named rare-earth engineering, which leads to quite different quantum transport behaviors[34,35]. In particular, $TbMn_6Sn_6$ shows an out-of-plane magnetization and stands out as a Chern insulator with zero-field anomalous Hall, anomalous Nernst, and anomalous thermal Hall effects[10,35–37]. For REV_6Sn_6 compounds with similar crystal structure yet featuring a nonmagnetic vanadium-kagome lattice, weak magnetic couplings among the local 4*f* moments of various rare-earth atoms not only result in various magnetic orderings[38–40], but also in topologically nontrivial Dirac surface states (GdV_6Sn_6 and HoV_6Sn_6[41–43]), quantum oscillations (YV_6Sn_6[42]), quantum critical behavior (YbV_6Sn_6[44]), and charge density waves (ScV_6Sn_6[45–47]). The close relationship between rare-earth magnetism and topological electronic structure underscores that rare-earth engineering is an effective way to tune the exotic topological phases[35,48–50].

Recently, the nonmagnetic AM_3X_5 family (A = K, Rb, and Cs; M = Ti, V; X = Sb, Bi) with vanadium/titanium-kagome lattices[51,52] has aroused great interest due to the combined charge density wave states, superconductivity, orbital-selective nematic order or electronic nematicity, and nontrivial band topology[53–60]. By intercalating RE ions between VSb layers, vanadium-based kagome metals with multiple magnetic states emerge[61], such as a FM-like ground state in EuV_3Sb_4. In contrast, there is a lack of systematic investigation into titanium-based kagome metals with magnetism, only $LaTi_3Bi_4$, $CeTi_3Bi_4$[62], and $EuTi_3Bi_4$[63] have been briefly reported.

By using rare-earth engineering, we report the synthesis and physical properties of three discovered titanium-based kagome metals, $RETi_3Bi_4$ (RE = Yb, Pr, and Nd). Compared with AM_3X_5, the titanium-kagome lattice in $RETi_3Bi_4$ is slightly distorted, and zig-zag RE chains are formed in REBi bilayers, enabling the exhibition of various magnetic states with different RE atoms. The combined measurements of magnetism, resistivity, and specific heat capacity show an evolution from the nonmagnetic $YbTi_3Bi_4$ to short-range ordered $PrTi_3Bi_4$, with an anomaly around 8.2 K, and finally to FM $NdTi_3Bi_4$, with $T_c = 8.5$ K. Applying pressure slightly suppressed the FM order in $NdTi_3Bi_4$, with an increasing value of power, showing the tunable magnetism. Therefore, $RETi_3Bi_4$ (RE = Yb, Pr, and Nd) represents a promising family of kagome metals for in-depth investigation of the interplay among topologically nontrivial features, magnetism, and electron correlation.

Results and Discussion

Crystal structure

Unlike the hexagonal prototypes AM_3X_5 (A = K, Rb, and Cs; M = Ti, V; X = Sb, Bi)[51,52,60], all $RETi_3Bi_4$ crystallize in the orthogonal space group *Fmmm* (No. 69) with $a = 24.9(4)$ Å, $b = 10.3(4)$ Å, $c = 5.9(2)$ Å for $YbTi_3Bi_4$; $a = 24.9668(114)$ Å, $b = 10.3248(49)$ Å, $c = 5.9125(26)$ Å for $PrTi_3Bi_4$; $a = 24.9523(87)$ Å, $b = 10.3327(27)$ Å, $c = 5.9009(18)$ Å for $NdTi_3Bi_4$, and $\alpha = \beta = \gamma = 90°$ (Supplementary Table 1–5). As shown in Fig. 1a, the crystal structure consists of the alternating stacking of REBi, TiBi, and Bi layers along the *a* axis. Viewed along the *a* axis, a Ti kagome-like lattice and two Bi honeycomb-like lattices can be further resolved (Fig. 1b). There are two distinct differences between the crystal structure of AM_3X_5 and $RETi_3Bi_4$, i.e. (i) the increase of the *a* axis owing to the stacking of (ii) distorted TiBi layer with distorted Ti kagome lattice. Compared with ATi_3Bi_5, the Ti kagome lattice and Bi triangular lattice of $RETi_3Bi_4$ show inequivalent bonds and are not strictly in the *bc* plane, resulting in both in-plane and out-of-plane distortion of TiBi layer. The in-plane distortion can be simply evaluated by the orthorhombic lattice parameter ratio *b*/*c*, which should be the exact value of $\sqrt{3} = 1.732$ for a perfect kagome lattice. For rare earth atoms shifting from Yb to Pr, and then to Nd, the orthorhombic lattice parameter ratio *b*/*c* changes from 1.7457 to 1.7462, and then to 1.7510, indicating a slight increase in the in-plane distortion. Similar to LnV_3Sb_4 (Ln = Yb, Eu)[61], the bilayer of the REBi plane forms a quasi-one-dimensional zig-zag chain of RE atoms (Fig. 1c), on which the magnetic states could be tuned by rare-earth engineering.

The crystal structure is further confirmed by the X-ray diffraction patterns, which show a strong preferential orientation of (00 *l*) (*l* = even integer) reflections (Fig. 2a). Based on the position (~14.3°) of (004) diffraction peaks, the distance between corresponding structural units along the *a* axis is determined to be about 25 Å, close to the results of Single crystal X-ray diffraction (SCXRD). As shown in the insets of Fig. 2a, the as-grown single crystals of $RETi_3Bi_4$ are all plate-like flakes with shiny metal luster, indicating a clear quasi-two-dimensional feature. Fig. 2b shows the enlarged (0010) diffraction peaks for $RETi_3Bi_4$, where the peak position of $PrTi_3Bi_4$ shifts 0.08° to a lower angle and that of $NdTi_3Bi_4$ shifts 0.06° to a higher angle compared to $YbTi_3Bi_4$, indicating the largest distance between the structural units for $PrTi_3Bi_4$ and the smallest one for $NdTi_3Bi_4$. The different (0010) peak position corresponds well with the lattice parameter derived from SCXRD, where $a(NdTi_3Bi_4) < a(YbTi_3Bi_4) < a(PrTi_3Bi_4)$. Considering the cationic radius $r(Yb^{3+}) = 0.0858$ nm $< r(Yb^{2+}) = 0.093$ nm $< r(Nd^{3+}) = 0.0995$ nm $< r(Pr^{3+}) = 0.1013$ nm, the abnormal enhancement of lattice parameter *a* in $YbTi_3Bi_4$ might be attributed to the weakened out-of-plane interaction between YbBi bilayer with Yb^{2+} ions rather than Yb^{3+} ions. As shown in the selected area electron diffraction (SAED) pattern and high-angle annular dark-field (HAADF) image of $YbTi_3Bi_4$ collected along the [0–26] zone axis (Fig. 2c, d), the construction layers can be clearly resolved along the *a* axis. In particular, the Ti atoms and Bi atoms are not on the same straight line, further confirming the out-of-plane distortion of TiBi layers. The chemical composition is determined to be RE: Ti: Bi ~1: 3: 4 with a homogeneous distribution according to the results of energy-dispersive spectroscopy (EDS) (Supplementary Fig. 1-2 and Supplementary Table 6–8).

Magnetic properties

Figure 3a–c shows the magnetic susceptibility of $RETi_3Bi_4$ under field parallel (H // bc) and normal ($H \perp bc$) to the *bc* plane. The in-plane (H // bc) magnetic susceptibilities are larger than the out-of-plane ($H \perp bc$) magnetic susceptibilities, showing the possible in-plane magnetic anisotropy in these three compounds. For $YbTi_3Bi_4$, the zero-field-cooling (ZFC) and field-cooling (FC) curves under a smaller magnetic field (0.5 T) exhibit no bifurcation or anomaly above 2 K, suggesting there is no magnetic transition above

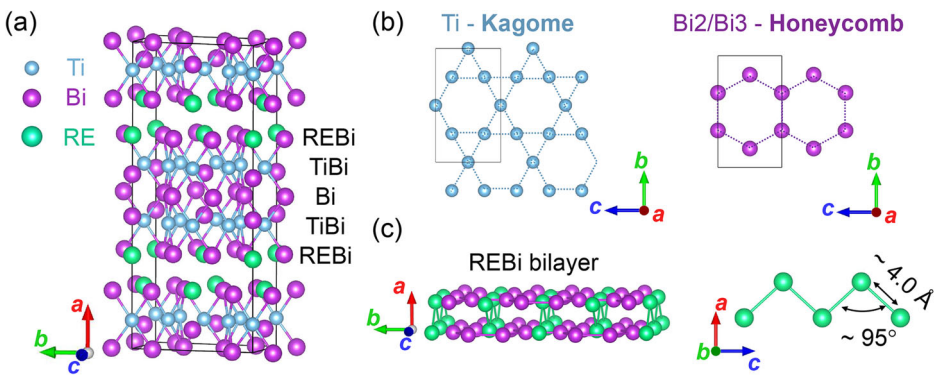

Fig. 1 | Crystal structure of $RETi_3Bi_4$ (RE = Yb, Pr, and Nd). a Crystal structure of $RETi_3Bi_4$ (RE = Yb, Pr, and Nd). **b** The Ti kagome-like lattice and Bi honeycomb-like lattices viewed along the *a* axis. **c** The REBi bilayer and zig-zag chain of RE atoms.

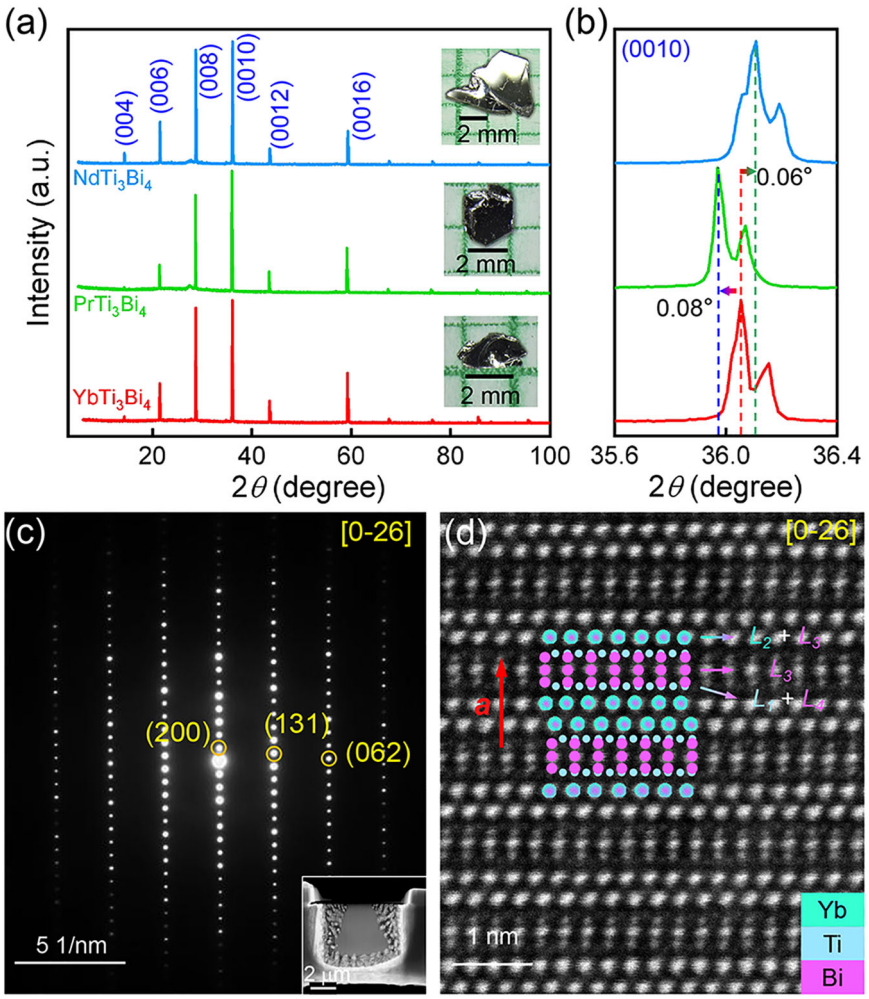

Fig. 2 | Single Crystals of $RETi_3Bi_4$ (RE = Yb, Pr, and Nd). **a** X-ray diffraction patterns of as-grown $RETi_3Bi_4$ (RE = Yb, Pr, and Nd) single crystals, showing (00 *l*) (*l* = even integer) reflections. The insets are the corresponding optical photographs of $RETi_3Bi_4$ (RE = Yb, Pr, and Nd) single crystals. **b** The enlarged (0010) peak of $RETi_3Bi_4$ (RE = Yb, Pr, and Nd) single crystals. **c** The SAED pattern of $YbTi_3Bi_4$ along the[0–26] zone axis. The inset is the thin specimen of $YbTi_3Bi_4$ etched by focused ion beam method. **d** The HAADF image collected along the[0–26] zone axis, where the cyan, blue, and purple balls represent Yb, Ti, and Bi atoms, respectively.

2 K. Though without bifurcation in the ZFC and FC curves under the smaller magnetic field (0.5 T) above 2 K, a saturation tendency appears at low temperature in the magnetic susceptibility of $PrTi_3Bi_4$ for both H // bc and $H \perp bc$, possibly indicating a short-range ordering around $T_{anomaly} \sim 8.2$ K (Supplementary Fig. 3). By contrast, a bifurcation around 8.5 K (denoted as T_c) can be clearly resolved in the ZFC and FC curves for $NdTi_3Bi_4$.

All the magnetic susceptibility curves decrease quickly around 20 K and follow the Curie-Weiss law at higher temperatures (black lines), given by $\chi = \chi_0 + C/(T - \theta_{CW})$, where χ_0 is the temperature-independent contribution including the diamagnetic contribution of the orbital magnetic moment (negative) and the Pauli paramagnetic contribution of conduction electrons (positive), C the Curie constant, and θ_{CW} the Curie-Weiss temperature. The effective moment can be further calculated from the equation $\mu_{eff} = \sqrt{\frac{8C}{n}}$, where n is the number of magnetic atoms. For $YbTi_3Bi_4$, an almost zero Curie-Weiss temperature (~0.5 K) and a small effective moment (<0.3 μ_B per Yb) were found for both H // bc and $H \perp bc$, indicating a possible non-magnetic ground state with zero spin (0 μ_B) Yb^{2+}. For $PrTi_3Bi_4$, a positive but close-to-zero Curie-Weiss temperature (~2.5 K) was determined for H // bc, which may suggest weak magnetic exchange couplings between moments in the bc plane. The effective moment was calculated to be 3.67(3) μ_B per Pr for H // bc, close to the theoretical moment of Pr^{3+} (3.58 μ_B). Shifting the magnetic field configuration into $H \perp bc$, the large negative Curie-Weiss temperature (−100 K) indicates strong antiferromagnetic interactions between moments in different Pr triangular bilayers along the a axis. The overestimated effective moment (4.72 μ_B per Pr) could possibly be attributed to geometrical spin frustration on the Pr triangular lattice or crystal field effect when considering the coordination environment of Pr atoms (Supplementary Fig. 4). By substituting Pr with Nd, a small negative Curie-Weiss temperature (−3.74 K) for H // bc also suggests weak magnetic exchange couplings between moments in the bc plane. Compared with $PrTi_3Bi_4$, the reduced Curie-Weiss temperature (−36.7 K) for $H \perp bc$ may correspond to a weakened antiferromagnetic interactions between different Nd triangular bilayers along the a axis, which might result in the emergence of FM order in $NdTi_3Bi_4$. The derived effective moments (~ 3.6 μ_B) of $NdTi_3Bi_4$ are close to the theoretical value of Nd^{3+} (3.62 μ_B). (For details of the Curie-Weiss fittings see Supplementary Table 9 and Supplementary Fig. 5-6.)

The magnetization curves of $YbTi_3Bi_4$ and $PrTi_3Bi_4$ show positive slopes and approach saturation around 7 T without any hysteresis (Fig. 3d, e), suggesting no FM order or spin-glass state at least above 2 K. The saturation moment for $YbTi_3Bi_4$ is 0.016 μ_B for H // bc and 0.006 μ_B for $H \perp bc$, further confirming the non-magnetic feature ($4f^{14}$, $\mu_{sat} = 0$ μ_B). The saturation moment for $PrTi_3Bi_4$ is 1.620 μ_B for H // bc and 0.855 μ_B for $H \perp bc$, with the former being close to the saturation moment of Pr^{3+} ($4f^2$, $\mu_{sat} = 2.0$ μ_B). The significant difference between the in-plane and out-of-plane saturation moments should be attributed to the large anisotropy originating from the quasi-two-dimensional structure. For $NdTi_3Bi_4$, obvious hysteresis loops exist at 2 K and gradually vanish beyond $T_c = 8.5$ K (Fig. 3f and Supplementary Fig. 7). The smaller in-plane coercive magnetic field ($H_{c-//} \sim 500$ Oe < $H_{c-\perp} \sim 5000$ Oe) and larger saturation moment ($\mu_{sat-//} \sim 1.426$ $\mu_B > \mu_{sat-\perp} \sim 0.587$ μ_B) suggest that the bc plane is the easy plane. For $NdTi_3Bi_4$, magnetization curves at various in-plane magnetic fields show the largest magnetization along the b axis (Supplementary Fig. 8-9), which should be the easy axis. Both the saturation moment and coercive magnetic field show a two-fold symmetry, corresponding to the quasi 1D arrangement of Nd atoms. Our

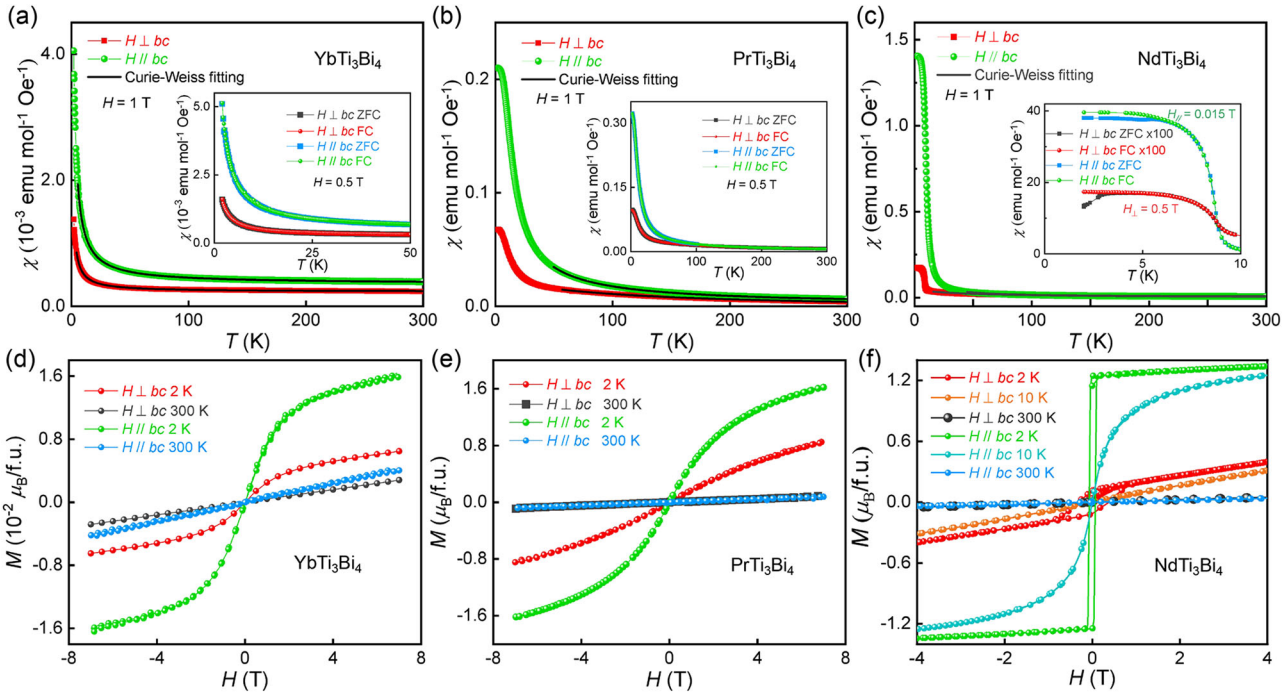

Fig. 3 | Various magnetic states of $RETi_3Bi_4$ (RE = Yb, Pr, and Nd). Temperature-dependent magnetic susceptibility of (**a**) $YbTi_3Bi_4$, (**b**) $PrTi_3Bi_4$, and (**c**) $NdTi_3Bi_4$ single crystal with magnetic field (1 T) parallel and perpendicular to the *bc* plane. The black lines are the Curie-Weiss fitting curves. The insets show the corresponding ZFC and FC curves under a smaller magnetic field. Field-dependent magnetization curves for (**d**) $YbTi_3Bi_4$, (**e**) $PrTi_3Bi_4$, and (**f**) $NdTi_3Bi_4$ single crystal with magnetic fields parallel and perpendicular to the *bc* plane.

results are consistent with those reported by a recently published work focusing on the evolution of highly anisotropic magnetism and complex electronic structure of the $RETi_3Bi_4$ family[64].

Resistivity and heat capacity

Figure 4a shows the temperature-dependent in-plane resistivity of $RETi_3Bi_4$, which monotonically decreases with decreasing temperature, demonstrating a metallic-like behavior (For the electronic structure of $PrTi_3Bi_4$ and $NdTi_3Bi_4$ see Supplementary Fig. 10). The residual resistance ratios ($RRR = \rho_{300\ K}/\rho_{10\ K}$) are calculated to be 3.50 for $YbTi_3Bi_4$, 2.15 for $PrTi_3Bi_4$, and 3.70 for $NdTi_3Bi_4$, hinting at the good crystallinity of $RETi_3Bi_4$ single crystals. With a current (2 mA) applied in the *bc* plane, the resistivity of $YbTi_3Bi_4$ shows no obvious anomaly down to 2 K. Unlike $YbTi_3Bi_4$, the in-plane resistivity of $PrTi_3Bi_4$ at low temperature exhibits an anomaly with a broadened peak (5.2 K ~ 9.7 K) in its first derivative curve (Supplementary Fig. 11), which might be correlated with the possible short-range order. Due to the obvious magnetic transition in $NdTi_3Bi_4$, the resistivity shows a distinct drop around $T_c = 8.5$ K and then approaches a saturation at 2 K. Similar to AV_3Sb_5 or ATi_3Bi_5, the resistivity of $RETi_3Bi_4$ below 50 K can be fitted using the Power law: $\rho = \rho_0 + AT^{\alpha}$, where the value of power α depends on the dominant scattering mechanism (Supplementary Table 10). Typically, α takes the value of 3/2 for diffusive electron motion caused by strong electron correlation[65], 2 for moderate electron-electron scattering[66,67], known as Fermi liquid behavior[68], 3 for dominant $s-d$ scattering or electron-magnon scattering[69–71], and 5 for electron-phonon coupling[72]. As shown in Fig. 4b, the value of power (α) is fitted to be 2.00(3) for $YbTi_3Bi_4$, 1.64(3) for $PrTi_3Bi_4$, and 1.51(2) for $NdTi_3Bi_4$, indicating an evolution of dominant scattering mechanism by changing rare earth atoms. In particular, the resistivity of $NdTi_3Bi_4$ below T_c can also be fitted using the Power law with $\alpha = 5.35(6)$, showing strong electron-phonon coupling below T_c. By applying a magnetic field perpendicular to the *bc* plane, the resistivity of $NdTi_3Bi_4$ below T_c shows a slight enhancement up to 5 T with almost unchanged transition temperature (Fig. 4c), which is a typical characteristic of FM order.

Figure 4d shows the temperature-dependent specific heat capacity of $RETi_3Bi_4$, where no anomaly in the entire measured temperature range, a broad anomaly around 8.2 K, and a sharp peak at $T_c = 8.5$ K is observed for $YbTi_3Bi_4$, $PrTi_3Bi_4$, and $NdTi_3Bi_4$, respectively. The specific heat capacity of all $RETi_3Bi_4$ single crystals exceed the Dulong–Petit limit ($3NR \sim 200$ J mol^{-1} K^{-1}, black dashed line) at higher temperatures, which should be attributed to the more prominent phonon contribution at higher temperature of N-type grease used for protecting the samples[73–75]. For $NdTi_3Bi_4$, the peak at 8.5 K is reversible upon cooling ($T\downarrow$) and warming ($T\uparrow$), indicating no structural transition. The low-temperature (12 K–18 K) specific heat capacity of $RETi_3Bi_4$ is fitted by the Debye model $C = \gamma T + \beta T^3$, where γT and βT^3 represent the contribution from the electron and lattice, respectively (Fig. 4e). The Sommerfeld coefficients γ are determined to be 33.5(2.6) mJ K^{-2} per formula for $YbTi_3Bi_4$ [20.7(7) mJ K^{-2} per formula fitted from 2 K to 5 K], 762.6(8.9) mJ K^{-2} per formula for $PrTi_3Bi_4$, and 809.6(7.5) mJ K^{-2} per formula for $NdTi_3Bi_4$. The large enhancement of Sommerfeld coefficient γ of $PrTi_3Bi_4$ and $NdTi_3Bi_4$ likely results from the contribution of magnons beyond the ordering temperatures. Taking the nonmagnetic $YbTi_3Bi_4$ as the reference of specific heat capacity contributed by electrons and phonons, the contribution of magnons and magnetic entropy of $PrTi_3Bi_4$ and $NdTi_3Bi_4$ are calculated (Supplementary Fig. 12), suggesting possible Pr^{3+} and Nd^{3+} valance states in $PrTi_3Bi_4$ and $NdTi_3Bi_4$, respectively. The λ-shaped peak of specific heat capacity for $NdTi_3Bi_4$ broadens and shifts toward higher temperature upon increasing the out-of-plane magnetic field (Fig. 4f), further confirming the FM order of $NdTi_3Bi_4$. Thus, various magnetic ground states have been realized in titanium-based kagome metals $RETi_3Bi_4$ through rare earth engineering, which so far includes nonmagnetic ($YbTi_3Bi_4$), possibly short-range ordered ($PrTi_3Bi_4$), and FM ($NdTi_3Bi_4$) states.

Resistance under high pressure for $NdTi_3Bi_4$

Upon applying hydrostatic pressure, multiple superconducting domes can be induced in AV_3Sb_5, illustrating the competition between charge density wave and superconductivity[76–78]. To explore potential superconductivity

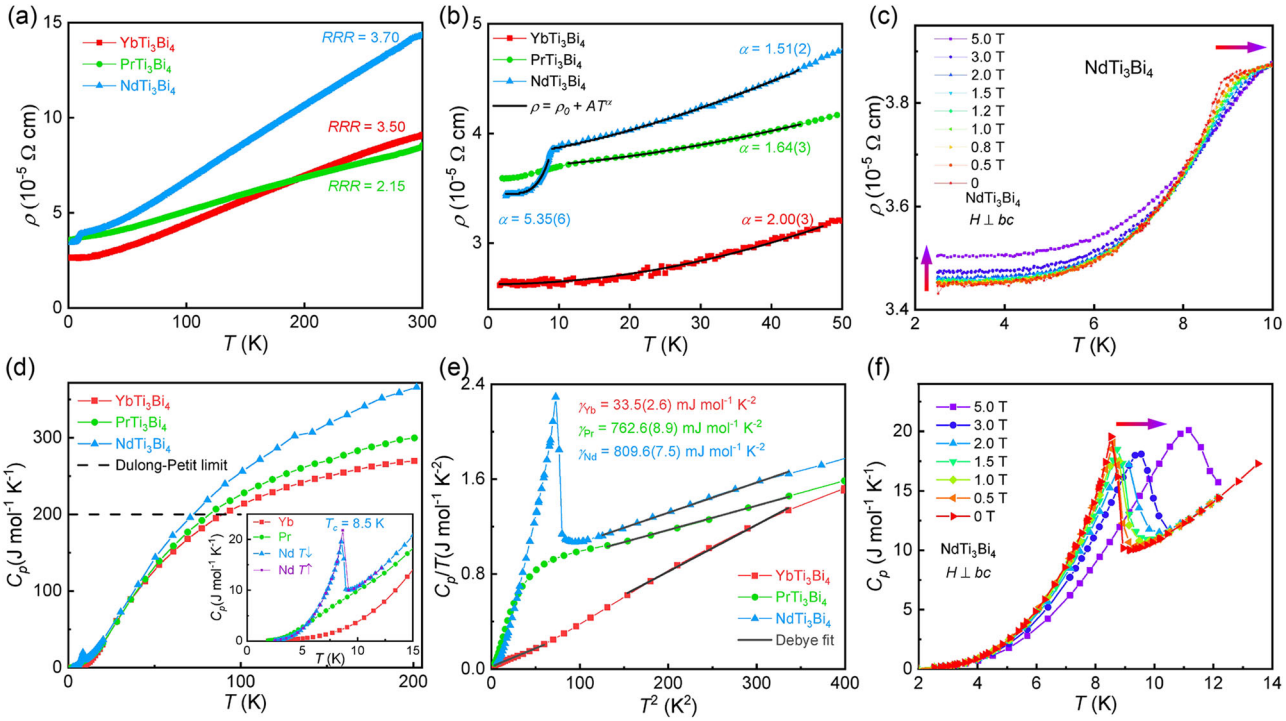

Fig. 4 | Electrical transport and specific heat capacity of $RETi_3Bi_4$ (RE = Yb, Pr, and Nd). **a** Temperature-dependent in-plane resistivity (ρ_{bc}) of $RETi_3Bi_4$ (RE = Yb, Pr, and Nd). **b** Power-law fittings of in-plane resistivity at low temperature. **c** In-plane resistivity of $NdTi_3Bi_4$ at low temperature under different magnetic field. **d** Temperature-dependent specific heat capacity of $RETi_3Bi_4$ (RE = Yb, Pr, and Nd). The inset shows zoomed specific heat capacity at low temperature. The black dashed line shows the Dulong-Petit limit of $RETi_3Bi_4$ compounds. **e** C_P/T *vs.* T^2 plot for $RETi_3Bi_4$ (RE = Yb, Pr, and Nd) and corresponding fittings (black lines) using the Debye model. **f** Zoomed specific heat capacity of $NdTi_3Bi_4$ at low temperature under different magnetic field.

and the evolution of magnetism, in situ resistance measurements of $NdTi_3Bi_4$ in the pressure range of 1.5 GPa to 41.9 GPa were performed using a diamond-anvil cell (Fig. 5a, b). Up to 10.2 GPa, a small drop related to FM order can be observed in resistance, with a superconducting-like transition occurring beyond 3.8 GPa (inset of Fig. 5a), where both the FM ordering temperature and superconducting transition temperature are suppressed as the pressure increases (Supplementary Fig. 13). By increasing the pressure beyond 10.2 GPa, the drop related to FM order becomes unresolved because the superconducting transition temperature suddenly rises. Until the pressure reaches 28.1 GPa, the drop related to FM order reappears due to the quicker suppression of superconducting transition. However, zero resistance is not observed in any measured curves, which may hint a nonintrinsic superconducting transition. Upon carefully evaluating the upper critical field (Supplementary Fig. 14), the superconducting signals should be attributed to three pressure-induced Bi phases (Bi-II, Bi-III, and Bi-V)[79], likely resulting from the remaining flux droplets or being induced by pressure in this Bi-rich compounds. Despite the superconducting side phase, the resistance of $NdTi_3Bi_4$ beyond FM ordering temperature (10 K–45 K) still follows the Power law, $R = R_0 + AT^{\alpha}$ (Supplementary Table 11). Fig. 5c illustrates the pressure dependence of fitted parameters and FM ordering temperature of $NdTi_3Bi_4$. The residual resistance (R_0) increases monotonically with pressure, whereas the decreasing correlation coefficient (A), increasing value of power (α), and decreasing FM ordering temperature (T_c) all exhibit a saturation tendency as pressure exceeds ~20 GPa. The FM ordering temperature decrease from 8.5 K (0 GPa) to ~6 K (> 20 GPa), demonstrating the tunability of ferromagnetism. Unlike directly changing the magnetic moments of RE atoms, hydrostatic pressure tunes the distance between RE atoms, affecting the magnetic exchange interaction and consequently the FM ordering temperature.

Conclusions

In summary, three titanium-based kagome metals, $RETi_3Bi_4$ (RE = Yb, Pr, and Nd) have been reported. Various magnetic states have been realized, including the nonmagnetic $YbTi_3Bi_4$, paramagnetic-like $PrTi_3Bi_4$ with an anomaly around $T_{anomaly}$ ~ 8.2 K, and FM $NdTi_3Bi_4$ with T_c = 8.5 K, indicating rare-earth engineering as an effective strategy to explore materials and tune their properties. Particularly for $NdTi_3Bi_4$, the FM ordering temperature is suggested to be tunable under high pressure. According to the crystal structure and magnetic properties, the materials can be simplified as distorted Ti atomic kagome bilayers with zig-zag rare earth atomic chains intercalated. Specifically, magnetism can be further tuned by changing the rare earth elements or applying external pressure. This work extends the $RETi_3Bi_4$ family with diverse magnetic states a promising platform to investigate the interplay between topologically nontrivial features, magnetism, and electron correlation. Further calculations and experimental characterizations, such as anisotropic magnetism or magnetoresistance, angle-resolved photoemission spectroscopy, and scanning tunneling microscopy or spectroscopy, are all desired to unravel the potential exotic topological phases of titanium-based kagome metals $RETi_3Bi_4$.

Note added: During the submission process of this manuscript, several related works were posted on arXiv[80–84] and published[64] within a short period of time, showcasing the $RETi_3Bi_4$ family as an excellent platform for exploring kagome materials.

Methods

Single crystal growth

$RETi_3Bi_4$ (RE = Yb, Pr, and Nd) single crystals were grown by a high-temperature solution method using Bi as flux. The as-received Yb/Pr/Nd ingot (99.9%, Alfa Aesar) was cut into small pieces, then mixed with Ti powder (99.95%, Alfa Aesar) and Bi granules (99.999%, Sinopharm) with a molar ratio of Yb/Pr/Nd: Ti: Bi = 2: 4: 12 in a fritted alumina crucible set (Canfield crucible set)[85] and sealed in a fused-silica ampoule under vacuum. The ampoule was heated to 1073 K over 15 h, held at the temperature for 24 h, and then slowly cooled down to 873 K at a rate of 2 K/h. At 873 K, hexagonal-shaped, shiny-silver single crystals with sizes up to 5 mm × 5 mm × 0.5 mm were separated from the remaining liquid by centrifuging the

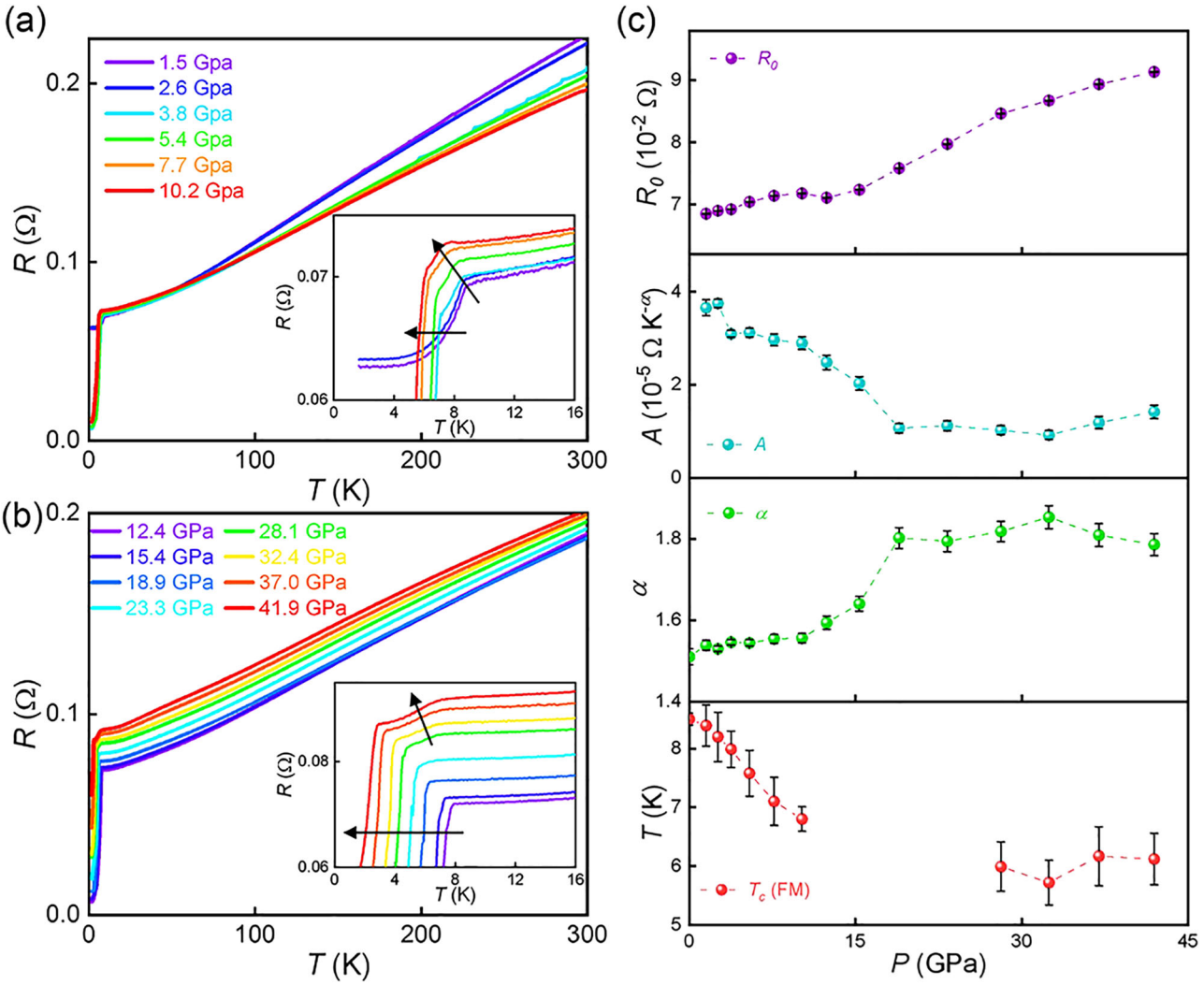

Fig. 5 | Magnetism tuned by pressure. Temperature-dependent resistance of $NdTi_3Bi_4$ under pressure from (**a**) 1.5 GPa to 10.2 GPa, and (**b**) 12.4 GPa to 41.9 GPa. The insets show the resistance at low temperature ranging from 1.7 K to 12 K. The arrows show the suppression trend of FM ordering temperature of $NdTi_3Bi_4$ and superconducting transition temperature of Bi. **c** The evolution of fitted parameters of resistance at low temperature using Power law fitting $R = R_0 + AT^{\alpha}$ and FM ordering temperature of $NdTi_3Bi_4$ under pressure. The error bars of R_0, A and are determined by the standard error of Power law fitting and the error bar of T_c is denoted by the half-height width of the peak in the first derivative curves of resistance (dR/dT).

ampoule. Considering the potential air sensitivity of the surface, all manipulations and specimen preparation for structure characterization and property measurements were handled in an argon-filled glove box.

Structure characterization and composition analysis

X-ray diffraction data were obtained using a PANalytical X'Pert PRO diffractometer (Cu K_α radiation, λ = 1.54178 Å) operated at 40 kV voltage and 40 mA current, with a graphite monochromator in a reflection mode (2θ = 5°–100°, step size = 0.017°). Indexing and Rietveld refinement were performed using the DICVOL91 and FULLPROF programs[86]. SCXRD data were collected using a Bruker D8 VENTURE with Mo K_α radiation (λ = 0.71073 Å) at 280 K for $PrTi_3Bi_4$ and $NdTi_3Bi_4$. The structure was solved using a direct method and refined with the Olex2[87] and Jana2020[88] packages. Due to the air sensitivity and two-dimensional feature of $YbTi_3Bi_4$, its crystal structure cannot be determined solely by SCXRD. The focused ion beam method was used to prepare thin specimens of $YbTi_3Bi_4$ with a thickness of ~50 nm for scanning transmission electron microscopy analysis. The crystal structure of $YbTi_3Bi_4$ was characterized by high-angle annular dark-field (HAADF) images obtained using a JEOL ARM-200F transmission electron microscope with double Cs correctors for the condenser and objective lens. The available spatial resolution is better than 78 picometers at 200 kV. The morphology and elemental analyses were characterized using a scanning electron microscope (SEM-4800, Hitachi) equipped with an electron microprobe analyzer for semi-quantitative elemental analysis in EDS mode. Three spots in three different locations were measured on each crystal using EDS.

Physical property measurements

Temperature-dependent magnetic susceptibility was measured using a vibrating sample magnetometer system (Quantum Design) under a magnetic field of 0.5 T parallel (H // bc) and normal ($H \perp bc$) to the bc plane using both the ZFC and FC protocols. Only magnetic susceptibility in FC protocol was measured under a larger field (1 T), and the field-dependent magnetization curves were measured under the magnetic field up to 7 T parallel and perpendicular to the bc plane. The resistivity and heat capacity measurements were carried out using a physical property measurement system (Quantum Design, 9 T). Resistivity was measured using the standard four-probe configuration with the applied current (about 2 mA) parallel to the bc plane. Heat capacity measurement was carried out at a temperature ranging from 2.2 K to 200 K at high vacuum (0.01 μbar). To protect the sample from air and moisture, thin film of N-type grease (~0.05 mg) was spread to cover the sample in an argon-

filled glove box. Subsequently, the sample was mounted on the square plate of specialized heat capacity pucks in air.

In-situ high-pressure resistance measurement

The standard four-probe resistance measurement under high pressure for the $NdTi_3Bi_4$ sample was carried out at high-pressure synergetic measurement station, synergetic extreme condition user facility. A Cu-Be alloy diamond-anvil cell with a 300 μm diamond culet in diameter was used. For the sample chamber, a 100 μm diameter hole was drilled in a rhenium gasket with a c-BN insulating layer, which was then filled with KBr as the pressure-transmitting medium. A long-stick-shaped $NdTi_3Bi_4$ single crystal sample was loaded into the sample chamber in an argon-filled glove box. Four Pt electrodes were contacted to the sample in the four-probe configuration. The pressure in the sample chamber could be calibrated by ruby fluorescence at room temperature.

First principles calculations

First principles calculations were carried out with the projector augmented wave method as implemented in the Vienna ab initio simulation package[89–91]. The generalized gradient approximation[92] of the Perdew-Burke-Ernzerhof[90] type was adopted for the exchange-correlation function. The cutoff energy of the plane-wave basis was 500 eV and the energy convergence standard was set to 10^{-8} eV. The $3 \times 11 \times 4$ Monkhorst-Pack K-point mesh was employed for the Brillouin zone sampling of the $1 \times 1 \times 1$ unit cell. Since Bi is a quite heavy element, spin-orbit coupling was taken into account by treating core electrons in fully relativistic method and valance electrons in second-variation method.

Data availability

The data that support the findings of this study are available from the corresponding author upon reasonable request.

Received: 17 December 2023; Accepted: 26 April 2024;
Published online: 10 May 2024

References

1. Yin, J. X., Lian, B. & Hasan, M. Z. Topological kagome magnets and superconductors. *Nature* **612**, 647–657 (2022).
2. Heisenberg, W. Zur Theorie des Ferromagnetismus. *Zeitschrift für Physik* **49**, 619–636 (1928).
3. Syôzi, I. Statistics of Kagomé Lattice. *Progr. Theor. Phys.* **6**, 306–308 (1951).
4. Yan, S., Huse, D. A. & White, S. R. Spin-liquid ground state of the S = 1/2 kagome Heisenberg antiferromagnet. *Science* **332**, 1173–1176 (2011).
5. Han, T. H. et al. Fractionalized excitations in the spin-liquid state of a kagome-lattice antiferromagnet. *Nature* **492**, 406–410 (2012).
6. Anderson, P. W. Resonating valence bonds: A new kind of insulator? *Mater. Res. Bull.* **8**, 153–160 (1973).
7. Broholm, C. et al. Quantum spin liquids. *Science* **367**, eaay0668 (2020).
8. Mielke, A. Ferromagnetic ground states for the Hubbard model on line graphs. *J. Phys. A Mathe. General* **24**, L73 (1991).
9. Ye, L. et al. Massive Dirac fermions in a ferromagnetic kagome metal. *Nature* **555**, 638–642 (2018).
10. Yin, J.-X. et al. Quantum-limit Chern topological magnetism in $TbMn_6Sn_6$. *Nature* **583**, 533–536 (2020).
11. Wang, W.-S., Li, Z.-Z., Xiang, Y.-Y. & Wang, Q.-H. Competing electronic orders on kagome lattices at van Hove filling. *Phys. Rev. B* **87**, 115135 (2013).
12. Guo, H. M. & Franz, M. Topological insulator on the kagome lattice. *Phys. Rev. B* **80**, 113102 (2009).
13. Tang, E., Mei, J.-W. & Wen, X.-G. High-Temperature Fractional Quantum Hall States. *Phys. Rev. Lett.* **106**, 236802 (2011).
14. Xu, G., Lian, B. & Zhang, S.-C. Intrinsic Quantum Anomalous Hall Effect in the kagome Lattice $Cs_2LiMn_3F_{12}$. *Phys. Rev. Lett.* **115**, 186802 (2015).
15. Liu, E. et al. Giant anomalous Hall effect in a ferromagnetic kagome-lattice semimetal. *Nat. Phys.* **14**, 1125–1131 (2018).
16. Kida, T. et al. The giant anomalous Hall effect in the ferromagnet Fe_3Sn_2—a frustrated kagome metal. *J. Phys. Conden. Matter* **23**, 112205 (2011).
17. Weyl, H. Elektron und Gravitation. I. *Zeitschrift für Physik* **56**, 330–352 (1929).
18. Wan, X., Turner, A. M., Vishwanath, A. & Savrasov, S. Y. Topological semimetal and Fermi-arc surface states in the electronic structure of pyrochlore iridates. *Phys. Rev. B* **83**, 205101 (2011).
19. Burkov, A. A. & Balents, L. Weyl Semimetal in a Topological Insulator Multilayer. *Phys. Rev. Lett.* **107**, 127205 (2011).
20. Halperin, B. I. Possible States for a Three-Dimensional Electron Gas in a Strong Magnetic Field. *Jap. J. Appl. Phys.* **26**, 1913 (1987).
21. Tomiyoshi, S. & Yamaguchi, Y. Magnetic Structure and Weak Ferromagnetism of Mn_3Sn Studied by Polarized Neutron Diffraction. *J. Phys. Soc. Japan* **51**, 2478–2486 (1982).
22. Yang, H. et al. Topological Weyl semimetals in the chiral antiferromagnetic materials Mn_3Ge and Mn_3Sn. *New J. Phys.* **19**, 015008 (2017).
23. Nayak, A. K. et al. Large anomalous Hall effect driven by a nonvanishing Berry curvature in the noncolinear antiferromagnet Mn_3Ge. *Sci. Adv.* **2**, e1501870 (2016).
24. Wang, Q. et al. Large intrinsic anomalous Hall effect in half-metallic ferromagnet $Co_3Sn_2S_2$ with magnetic Weyl fermions. *Nat. Commun.* **9**, 3681 (2018).
25. Morali, N. et al. Fermi-arc diversity on surface terminations of the magnetic Weyl semimetal $Co_3Sn_2S_2$. *Science* **365**, 1286–1291 (2019).
26. Liu, D. F. et al. Direct observation of the spin–orbit coupling effect in magnetic Weyl semimetal $Co_3Sn_2S_2$,. *npj Quantum Mater* **7**, 11 (2022).
27. Liu, Z. et al. Orbital-selective Dirac fermions and extremely flat bands in frustrated kagome-lattice metal CoSn. *Nat. Commun.* **11**, 4002 (2020).
28. Kang, M. et al. Topological flat bands in frustrated kagome lattice CoSn. *Nat. Commun.* **11**, 4004 (2020).
29. Fenner, L. A., Dee, A. A. & Wills, A. S. Non-collinearity and spin frustration in the itinerant kagome ferromagnet Fe_3Sn_2. *J. Phys. Conden. Matter* **21**, 452202 (2009).
30. Fang, S. et al. Ferromagnetic helical nodal line and Kane-Mele spin-orbit coupling in kagome metal Fe_3Sn_2. *Phys. Rev. B* **105**, 035107 (2022).
31. Sales, B. C. et al. Electronic, magnetic, and thermodynamic properties of the kagome layer compound FeSn. *Phys. Rev. Mater.* **3**, 114203 (2019).
32. Kang, M. et al. Dirac fermions and flat bands in the ideal kagome metal FeSn. *Nat. Mater.* **19**, 163–169 (2020).
33. Lin, Z. et al. Dirac fermions in antiferromagnetic FeSn kagome lattices with combined space inversion and time-reversal symmetry. *Phys. Rev. B* **102**, 155103 (2020).
34. Venturini, G., Idrissi, B. C. E. & Malaman, B. Magnetic properties of RMn_6Sn_6 (R = Sc, Y, Gd−Tm, Lu) compounds with $HfFe_6Ge_6$ type structure. *J. Magn. Magn. Mater.* **94**, 35–42 (1991).
35. Ma, W. et al. Rare Earth Engineering in RMn_6Sn_6 (R=Gd-Tm, Lu) Topological kagome Magnets. *Phys. Rev. Lett.* **126**, 246602 (2021).
36. Xu, X. et al. Topological charge-entropy scaling in kagome Chern magnet $TbMn_6Sn_6$. *Nature Communications* **13**, 1197 (2022).
37. Zhang, H. et al. Exchange-biased topological transverse thermoelectric effects in a kagome ferrimagnet. *Nature Communications* **13**, 1091 (2022).
38. Lee, J. & Mun, E. Anisotropic magnetic property of single crystals RV_6Sn_6 (R=Y, Gd-Tm, Lu). *Phys. Rev. Mater.* **6**, 083401 (2022).

39. Rosenberg, E. et al. Uniaxial ferromagnetism in the kagome metal TbV_6Sn_6. *Phys. Rev. B* **106**, 115139 (2022).
40. Zhang, X. et al. Electronic and magnetic properties of intermetallic kagome magnets RV_6Sn_6 (R=Tb-Tm). *Phys. Rev. Mater.* **6**, 105001 (2022).
41. Peng, S. et al. Realizing kagome Band Structure in Two-Dimensional kagome Surface States of RV_6Sn_6 (R=Gd, Ho). *Phys. Rev. Lett.* **127**, 266401 (2021).
42. Pokharel, G. et al. Electronic properties of the topological kagome metals YV_6Sn_6 and GdV_6Sn_6. *Phys. Rev. B* **104**, 235139 (2021).
43. Hu, Y. et al. Tunable topological Dirac surface states and van Hove singularities in kagome metal GdV_6Sn_6. *Sci. Adv.* **8**, eadd2024 (2022).
44. Guo, K., Ye, J., Guan, S. & Jia, S. Triangular Kondo lattice in YbV_6Sn_6 and its quantum critical behavior in a magnetic field. *Phys. Rev. B* **107**, 205151 (2023).
45. Hu, T. et al. Optical spectroscopy and band structure calculations of the structural phase transition in the vanadium-based kagome metal ScV_6Sn_6. *Phys. Rev. B* **107**, 165119 (2023).
46. Arachchige, H. W. S. et al. Charge Density Wave in kagome Lattice Intermetallic ScV_6Sn_6. *Phys. Rev. Lett.* **129**, 216402 (2022).
47. Zhang, X. et al. Destabilization of the Charge Density Wave and the Absence of Superconductivity in ScV_6Sn_6 under High Pressures up to 11 GPa. *Materials* **15**, 7372 (2022).
48. Chen, H. et al. Topological crystalline insulator candidate ErAsS with hourglass Fermion and magnetic-tuned topological phase transition. *Adv. Mater.* **34**, e2110664 (2022).
49. Kang, B. et al. Giant negative magnetoresistance beyond Chiral anomaly in topological material $YCuAs_2$. *Adv. Mater. (Weinheim, Ger.)* **34**, 2201597 (2022).
50. Chen, L. et al. Large negative magnetoresistance beyond chiral anomaly in topological insulator candidate $CeCuAs_2$ with spin-glass-like behavior. *The Innovation Materials*. **1**, 100011 (2023).
51. Ortiz, B. R. et al. New kagome prototype materials: discovery of KV_3Sb_5, RbV_3Sb_5, and CsV_3Sb_5. *Phys. Rev. Mater.* **3**, 094407 (2019).
52. Werhahn, D. et al. The kagomé metals $RbTi_3Bi_5$ and $CsTi_3Bi_5$,. *Z. Naturforsch. B* **77**, 757–764 (2022).
53. Cho, S. et al. Emergence of new van Hove singularities in the charge density wave state of a topological kagome metal RbV_3Sb_5. *Phys. Rev. Lett.* **127**, 236401 (2021).
54. Ortiz, B. R. et al. Superconductivity in the Z_2 kagome metal KV_3Sb_5. *Phys. Rev. Mater.* **5**, 034801 (2021).
55. Yin, Q. W. et al. Superconductivity and normal-state properties of kagome metal RbV_3Sb_5 single crystals. *Chin. Phys. Lett.* **38**, 037403 (2021).
56. Ortiz, B. R. et al. CsV_3Sb_5: A Z_2 topological kagome metal with a superconducting ground state. *Phys. Rev. Lett.* **125**, 247002 (2020).
57. Li, H. et al. Electronic nematicity in the absence of charge density waves in a new titanium-based kagome metal. *Nat. Phys.* **19**, 1591–1598 (2023).
58. Yang, H. et al. Titanium-based kagome superconductor $CsTi_3Bi_5$ and topological states, *arXiv*:2209.03840v1, https://doi.org/10.48550/arXiv.2209.03840 (2022).
59. Yang, H. et al. Superconductivity and orbital-selective nematic order in a new titaniumbased kagome metal $CsTi_3Bi_5$, *arXiv*:2211.12264v1, https://doi.org/10.48550/arXiv.2211.12264 (2022).
60. Zhou, Y. et al. Physical properties, electronic structure, and strain-tuned monolayer of the weak topological insulator $RbTi_3Bi_5$ with kagome lattice, *arXiv*:2301.01633, https://doi.org/10.48550/arXiv.2301.01633 (2023).
61. Brenden, G. P. et al. YbV_3Sb_4 and EuV_3Sb_4, vanadium-based kagome metals with Yb^{2+} and Eu^{2+} zig-zag chains,. *Phys. Rev. Mater.* **7**, 099901 (2023).
62. Motoyama, G. et al. Magnetic properties of new antiferromagnetic heavy-fermion compounds, Ce_3TiBi_5 and $CeTi_3Bi_4$. *Physica B* **536**, 142–144 (2018).
63. Ovchinnikov, A. & Bobev, S. Synthesis, Crystal and Electronic Structure of the Titanium Bismuthides $Sr_5Ti_{12}Bi_{19+x}$, $Ba_5Ti_{12}Bi_{19+x}$, and $Sr_{5-\delta}Eu_\delta Ti_{12}Bi_{19+x}$ ($x \approx 0.5$–1.0; $\delta \approx 2.4, 4.0$). *Euro. J. Inorg. Chem.* **2018**, 1266–1274 (2018).
64. Ortiz, B. R. et al. Evolution of Highly Anisotropic Magnetism in the Titanium-Based kagome Metals $LnTi_3Bi_4$ (Ln: La···Gd^{3+}, Eu^{2+}, Yb^{2+}). *Chem. Mater.* **35**, 9756–9773 (2023).
65. Pfleiderer, C., Julian, S. R. & Lonzarich, G. G. Non-Fermi-liquid nature of the normal state of itinerant-electron ferromagnets. *Nature* **414**, 427–430 (2001).
66. van der Marel, D., van Mechelen, J. L. M. & Mazin, I. I. Common Fermi-liquid origin of T^2 resistivity and superconductivity in n-type $SrTiO_3$. *Phys. Rev. B* **84**, 205111 (2011).
67. Baber, W. G. & Mott, N. F. The contribution to the electrical resistance of metals from collisions between electrons. *Proc Royal Soc. London. Series A - Mathe. Phys. Sci.* **158**, 383–396 (1937).
68. Abrikosov, A. A. & Khalatnikov, I. M. Theory of the Feimi fluid (The Properties of Liquid He3 at Low Temperatures). *Soviet Physics Uspekhi* **1**, 68 (1958).
69. Mott, N. F. Electrons in transition metals. *Adv. Phys.* **13**, 325–422 (1964).
70. Jiang, H. et al. Physical properties and electronic structure of $Sr_2Cr_3As_2O_2$ containing CrO_2 and Cr_2As_2 square-planar lattices. *Phys. Rev. B* **92**, 205107 (2015).
71. Wilson, A. H. & Fowler, R. H. The electrical conductivity of the transition metals. *Proc. Royal Soc. London. Series A. Mathe. Phys. Sci.* **167**, 580–593 (1938).
72. Luo, X. N. et al. Low-temperature physical properties and electronic structures of Ni_3Sb, Ni_5Sb_2, $NiSb_2$, and NiSb. *Chin. Phys. B* **24**, 067201 (2015).
73. Chen, L. et al. Quasi-one-dimensional structure and possible helical antiferromagnetism of $RbMn_6Bi_5$. *Inorg. Chem.* **60**, 12941–12949 (2021).
74. Zhou, Y. et al. A new superconductor parent compound $NaMn_6Bi_5$ with quasi-one-dimensional structure and lower antiferromagnetic-like transition temperatures. *Chin. Phys. Lett.* **39**, 047401 (2022).
75. Zhou, Y. et al. $ANi_5Bi_{5.6+\delta}$ (A = K, Rb, and Cs): Quasi-One-Dimensional Metals Featuring $[Ni_5Bi_{5.6+\delta}]^-$ Double-Walled Column with Strong Diamagnetism. *Inorg. Chem.* **62**, 3788–3798 (2023).
76. Chen, K. Y. et al. Double superconducting dome and triple enhancement of T_c in the kagome superconductor CsV_3Sb_5 under high pressure. *Phys. Rev. Lett.* **126**, 247001 (2021).
77. Chen, X. et al. Highly Robust Reentrant Superconductivity in CsV_3Sb_5 under Pressure. *Chin. Phys. Lett.* **38**, 057402 (2021).
78. Du, F. et al. Pressure-induced double superconducting domes and charge instability in the kagome metal KV_3Sb_5. *Phys. Rev. B* **103**, L220504 (2021).
79. Li, Y., Wang, E., Zhu, X. & Wen, H.-H. Pressure-induced superconductivity in Bi single crystals. *Phys. Rev. B* **95**, 024510 (2017).
80. Guo, J. et al. Magnetic kagome materials $RETi_3Bi_4$ family with weak interlayer interactions, arXiv preprint *arXiv*:2308.14509 https://doi.org/10.48550/arXiv.2308.14509 (2023).
81. Sakhya, A. P. et al. Observation of multiple flat bands and topological Dirac states in a new titanium based slightly distorted kagome metal $YbTi_3Bi_4$, *arXiv*:2309.01176v1 https://doi.org/10.48550/arXiv.2309.01176 (2023).
82. Hu, Y. et al. Magnetic-coupled electronic landscape in bilayer-distorted titanium-based kagome metals, *arXiv*:2311.07747 https://doi.org/10.48550/arXiv.2311.07747 (2023).
83. Mondal, M. I. et al. Observation of multiple van Hove singularities and correlated electronic states in a new topological ferromagnetic kagome metal $NdTi_3Bi_4$, *arXiv*:2311.11488 https://doi.org/10.48550/arXiv.2311.11488 (2023).

84. Zheng, Z. et al. Anisotropic magnetism and band evolution induced by ferromagnetic phase transition in titanium-based kagome ferromagnet $SmTi_3Bi_4$. *arXiv*:2308.14349., https://doi.org/10.48550/arXiv.2308.14349 (2023).
85. Canfield, P. C., Kong, T., Kaluarachchi, U. S. & Jo, N. H. Use of frit-disc crucibles for routine and exploratory solution growth of single crystalline samples. *Philosophical Magazine* **96**, 84–92 (2016).
86. Rodríguez-Carvajal J. FullProf[J]. CEA/Saclay, France, **1045**, 132–146 (2001).
87. Dolomanov, O. V., Bourhis, L. J., Gildea, R. J., Howard, J. A. K. & Puschmann, H. OLEX2: a complete structure solution, refinement and analysis program. *J. Appl. Crystallogr.* **42**, 339–341 (2009).
88. Petříček, V., Dušek, M. & Palatinus, L. Crystallographic Computing System JANA2006: General features. *Zeitschrift für Kristallographie - Crystal. Mater.* **229**, 345–352 (2014).
89. Kresse, G. & Hafner, J. Ab initio molecular-dynamics for liquid-metals. *Phys. Rev. B* **47**, 558–561 (1993).
90. Kresse, G. & Furthmuller, J. Efficiency of ab-initio total energy calculations for metals and semiconductors using a plane-wave basis set. *Comp. Mater. Sci.* **6**, 15–50 (1996).
91. Kresse, G. & Furthmuller, J. Efficient iterative schemes for ab initio total-energy calculations using a plane-wave basis set. *Phys. Rev. B* **54**, 11169–11186 (1996).
92. Perdew, J. P., Burke, K. & Ernzerhof, M. Generalized gradient approximation made simple. *Phys. Rev. Lett.* **78**, 1396 (1997).

Acknowledgements

L. Chen, Y. Zhou, and G. Wang would like to thank Prof. X. L. Chen, Prof. J. P. Hu, and Prof. T. Qian at the Institute of Physics, Chinese Academy of Sciences, and Prof. J. Ma at the Shanghai Jiao Tong University for helpful discussions. This work was partially supported by the Synergetic Extreme Condition User Facility (SECUF), the National Key Research and Development Program of China (Grant Nos. 2023YFA1607400, 2022YFA1403900, and 2018YFE0202600) and the National Natural Science Foundation of China (Grant No. 52325201, 51832010, and 11888101).

Author contributions

L.C., Y.Z., H.Z., and X.C.J. contributed equally to this work. X.H.Y., H.M.W. and G.W. conceived the project. L.C. and Y.Z. performed the crystal growth, structure, and physical properties characterization. H.Z. performed the high-pressure measurement. X.C.J. performed the first-principles calculations. K.L. and Y.L. prepared thin specimen using the focused ion beam method. X.S. and R.C.Y. performed the scanning transmission electron microscopy measurement. Z.N.G. and Y.J. helped in data analysis. All the authors co-wrote and revised the manuscript.

Competing interests

The authors declare no competing interests.

Additional information

Supplementary information The online version contains supplementary material available at https://doi.org/10.1038/s43246-024-00513-4.

Correspondence and requests for materials should be addressed to Xiaohui Yu, Hongming Weng or Gang Wang.

Peer review information *Communications Materials* thanks the anonymous reviewers for their contribution to the peer review of this work. Primary Handling Editor: Aldo Isidori. A peer review file is available.